ADVANCED MATERIALS
www.advmat.de

Rapid Regeneration of a Neoartery with Elastic Lamellae

*Ziyu Wang, Suzanne M. Mithieux, Howard Vindin, Yiwei Wang, Miao Zhang, Linyang Liu, Jacob Zbinden, Kevin M. Blum, Tai Yi, Yuichi Matsuzaki, Farshad Oveissi, Reyda Akdemir, Karen M. Lockley, Lingyue Zhang, Ke Ma, Juan Guan, Anna Waterhouse, Nguyen T. H. Pham, Brian S. Hawkett, Toshiharu Shinoka, Christopher K. Breuer, and Anthony S. Weiss**

Native arteries contain a distinctive intima-media composed of organized elastin and an adventitia containing mature collagen fibrils. In contrast, implanted biodegradable small-diameter vascular grafts do not present spatially regenerated, organized elastin. The elastin-containing structures within the intima-media region encompass the elastic lamellae (EL) and internal elastic lamina (IEL) and are crucial for normal arterial function. Here, the development of a novel electrospun small-diameter vascular graft that facilitates de novo formation of a structurally appropriate elastin-containing intima-media region following implantation is described. The graft comprises a non-porous microstructure characterized by tropoelastin fibers that are embedded in a PGS matrix. After implantation in mouse abdominal aorta, the graft develops distinct cell and extracellular matrix profiles that approximate the native adventitia and intima-media by 8 weeks. Within the newly formed intima-media region there are circumferentially aligned smooth muscle cell layers that alternate with multiple EL similar to that found in the arterial wall. By 8 months, the developed adventitia region contains mature collagen fibrils and the neoartery presents a distinct IEL with thickness comparable to that in mouse abdominal aorta. It is proposed that this new class of material can generate the critically required, organized elastin needed for arterial regeneration.

1. Introduction

Compromised arteries such as those apparent in severe atherosclerosis can result in myocardial infarction, which is the leading cause of death worldwide.[1] When required, a vascular graft can be used to repair the damaged artery. Autologous vascular grafts harvested from the saphenous veins, radial arteries, and internal mammary arteries of patients are considered gold-standard grafts. However, for patients with limited autologous graft availability due to pre-existing pathological conditions,[2] access to off-the-shelf synthetic grafts that exhibit similar durability to autologous grafts would provide alternative surgical options. Currently, commercially available synthetic grafts made from expanded polytetrafluoroethylene and poly(ethylene terephthalate) show markedly decreased patency over time when used as small-diameter vascular grafts (1–6 mm), due to thrombosis and

Z. Wang, S. M. Mithieux, H. Vindin, M. Zhang, L. Liu, K. M. Lockley, A. S. Weiss
School of Life and Environmental Sciences
University of Sydney
Sydney, NSW 2006, Australia
E-mail: tony.weiss@sydney.edu.au

Z. Wang, S. M. Mithieux, H. Vindin, M. Zhang, L. Liu, K. M. Lockley, A. Waterhouse, A. S. Weiss
Charles Perkins Centre
University of Sydney
Sydney, NSW 2006, Australia

The ORCID identification number(s) for the author(s) of this article can be found under https://doi.org/10.1002/adma.202205614.

DOI: 10.1002/adma.202205614

Y. Wang
Burns Research and Reconstructive Surgery
Anzac Research Institute
Sydney, NSW 2139, Australia

Y. Wang
Jiangsu Provincial Engineering Research Centre of TCM External Medication Development and Application
Nanjing University of Chinese Medicine
Nanjing, Jiangsu 210023, China

J. Zbinden, K. M. Blum, T. Yi, Y. Matsuzaki, T. Shinoka, C. K. Breuer
Center for Regenerative Medicine
Abigail Wexner Research Institute at Nationwide Children's Hospital
Columbus, OH 43215, USA

F. Oveissi
School of Chemical and Biomolecular Engineering
University of Sydney
Sydney, NSW 2006, Australia

R. Akdemir
Department of Chemical Engineering
University Rovira i Virgili
Tarragona E-43007, Spain

restenosis.[3] In addition, their non-degradable nature does not support complete arterial regeneration.

Engineered biodegradable vascular grafts, fabricated using a variety of techniques and materials, are being developed to address problems with patency and to deliver better tissue remodeling and regeneration outcomes.[4] Synthetic and natural polymers, with varying degradation times, have been used. Positive results have included robust mechanical performances with similar in vivo compliance to native blood vessels, and favorable biological outcomes, such as endothelium formation, smooth muscle cell (SMC) infiltration with proliferative to contractile phenotype conversion, and the deposition of extracellular matrix (ECM) proteins, particularly collagen and elastin.[2]

However, implanted biodegradable small-diameter vascular grafts do not present spatially regenerated, organized elastin, which prevents the appropriate arrangement of SMCs and endothelial cells (ECs), jeopardizing the graft's long-term performance.[5] There is thus an unmet demand for structural resemblance to the adjoining native artery, namely highly organized concentric layers of elastin alternating with SMC layers in the media, and hierarchically arranged collagen fibers in the adventitia. Organized elastin-based structures, such as the medial elastic lamellae (EL), internal elastic lamina (IEL), and external elastic lamina, naturally exist within the media region of the human artery and perform crucial functions such as conveying elasticity for vessel deformation during blood pressure changes and regulating arterial SMC phenotype in response to injury.[6] Previously developed vascular grafts have only shown limited elastin regeneration in the neoartery post implantation. Furthermore, this elastin has an amorphous morphology[7] randomly dispersed throughout the entire neoartery region, dissimilar to the continuous native EL that are only present within the intima-media. Direct incorporation of elastin fragments in grafts has also demonstrated limited success because these fragments are derived from degraded elastin,[8] in contrast to the use of full-length tropoelastin (TE), the ECM protein that is naturally used by elastogenic cells to make elastin.[5]

L. Zhang, K. Ma, J. Guan
International Research Center for Advanced Structural and Biomaterials
School of Materials Science and Engineering
Beihang University
Beijing 100191, China

A. Waterhouse
School of Medical Science
Faculty of Medicine and Health
University of Sydney
Sydney, NSW 2006, Australia

A. Waterhouse
The Heart Research Institute
University of Sydney
Sydney, NSW 204206, Australia

A. Waterhouse, B. S. Hawkett, A. S. Weiss
The University of Sydney Nano Institute
University of Sydney
Sydney, NSW 2006, Australia

N. T. H. Pham, B. S. Hawkett
Key Centre for Polymers and Colloids
School of Chemistry
University of Sydney
Sydney, NSW 2006, Australia

In this study, we fabricated a non-porous biodegradable vascular graft from a combination of TE and polyglycerol sebacate (PGS), a highly elastic and degradable biomaterial.[9] The presented data describe TE-PGS scaffold fabrication, characterization, selection, mouse abdominal aorta (AA) implantation, and remodeling into a neoartery. The non-porous fast-degrading vascular graft, TE50, acted as a framework on which the regeneration of organized EL and a distinct IEL occurred internally to the graft and an adventitia like structure containing collagen fibrils developed peripheral to the graft, resulting in marked spatial and microstructural resemblance to the native artery.

2. Results and Discussion

2.1. Generation of Electrospun TE-PGS Scaffolds with a Spectrum of Microstructures

To mimic the fibrous nature of the native artery, TE-PGS scaffolds were fabricated by electrospinning. PGS by itself cannot be readily electrospun[10] and mixing PGS with less than 20% w/v TE resulted in the assembly of droplet-like structures on the collector (Figure S1, Supporting Information). Mixing over 30% w/v TE with PGS in ratios of 30:70, 50:50, 70:30, and 100:0 TE:PGS resulted in the formation of electrospun scaffolds, which were named TE30, TE50, TE70, and TE100, respectively. A solvent cast PGS scaffold was used as a control, named PGS. All scaffolds were heat-stabilized at 160 °C for 16 h.[11] **Figure 1**A shows the morphologies of the scaffolds examined by scanning electron microscopy (SEM), which was used to characterize pore size and porosity. Before heat-stabilization, TE30 formed a solid non-porous structure whereas TE50, TE70, and TE100 formed fibrous porous structures. Heating did not affect the morphology of TE30 but resulted in a fiber-reinforced non-porous structure in TE50. The morphologies of TE70 and TE100 scaffolds were preserved after heating. TE70 showed a 26% and 21% reduction in pore size and porosity, respectively, while no changes were found for TE100 (Figure 1B,C).

The heat-stabilized scaffolds were examined by multiphoton microscopy to discern the individual microstructures of TE and PGS (Figure 1D). TE30 contained both TE aggregates and fibers embedded in a PGS matrix. TE50 showed homogeneously distributed TE fibers dispersed throughout a PGS matrix with a higher fiber network density compared to TE30. TE70 displayed a completely fibrous structure with both TE and PGS present in the same fibers and with the PGS component particularly concentrated at the interconnecting regions of the fibers. A fiber network structure was also observed for TE100. Both SEM and multiphoton characterization showed that electrospun TE-PGS scaffolds can exhibit a spectrum of microstructures, ranging from fiber-embedded non-porous matrices to complete fibrous networks, depending on the TE:PGS ratio.

2.2. Chemical and Mechanical Properties of Electrospun TE-PGS Scaffolds

Fourier transform infrared spectroscopy-attenuated total reflectance (FTIR-ATR) was used to assess the chemical composition

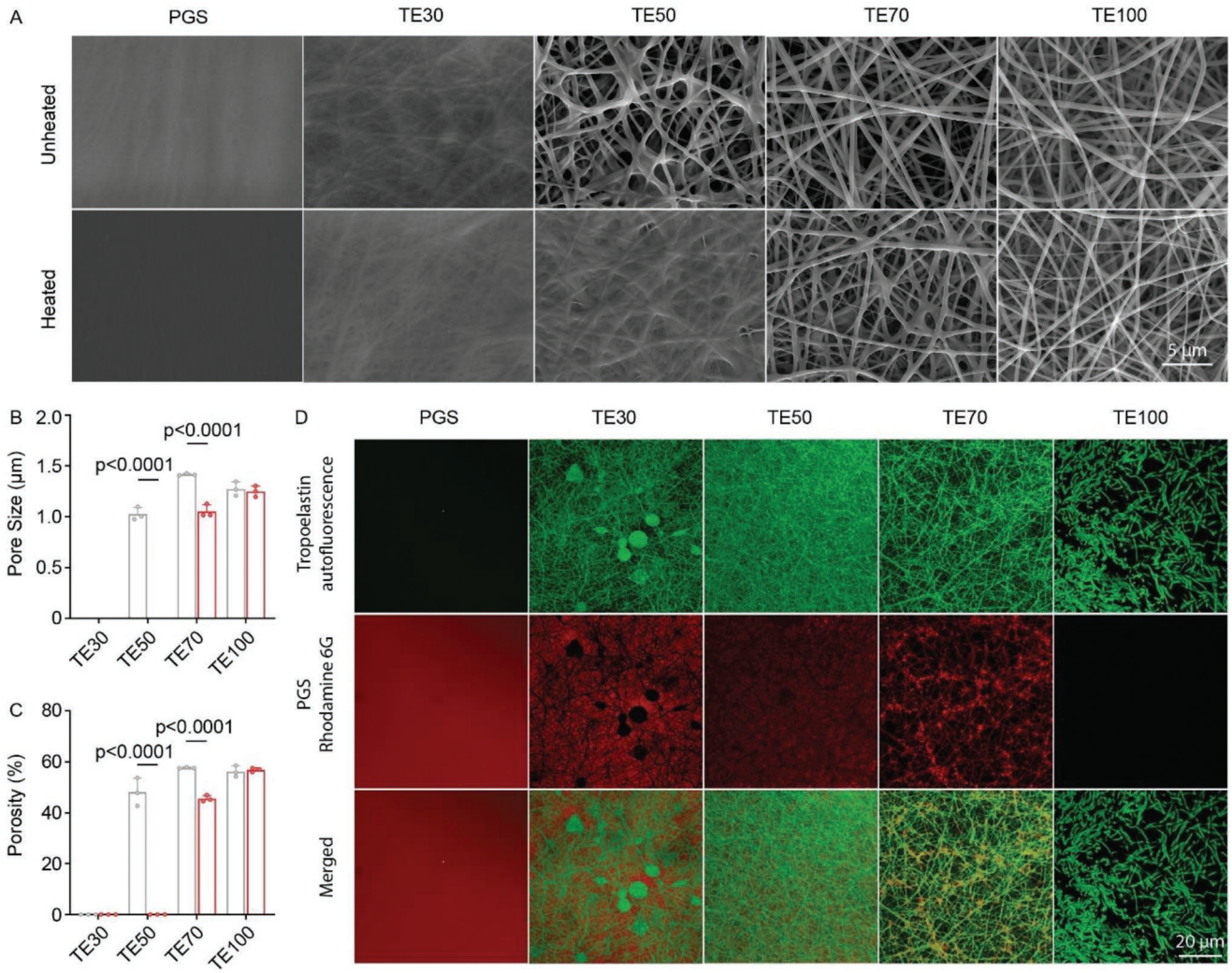

Figure 1. Microstructures of electrospun TE-PGS scaffolds. A) SEM images of unheated and heated PGS and electrospun TE-PGS scaffolds including TE30, TE50, TE70, and TE100. B) Pore size and C) porosity of unheated (gray), and heated (red) TE-PGS scaffolds determined from SEM images. D) Multiphoton microscopy images of heated PGS and electrospun TE-PGS scaffolds. Rhodamine 6G-stained PGS components are shown in red, TE autofluorescence is shown in green, and co-localized TE-PGS regions are shown in yellow. $n = 3$ for all quantitative experiments.

of the scaffolds before and after heat stabilization (**Figure 2**A). Peaks at 1733 and 1162 cm^{-1}, which represent ester bonds and C—O stretching bands present in PGS, and peaks at 1653 and 1545 cm^{-1}, which represent Amide I and Amide II protein bands, were observed for all electrospun TE-PGS scaffolds. No change in composition was seen after heat stabilization.

The stress–strain curve (Figure 2B) and relevant mechanical properties, including Young's modulus (Figure 2C), ultimate tensile strength (UTS) (Figure 2D), and elongation at break (Figure 2E) of TE-PGS scaffolds, were obtained through tensile testing. As the TE concentration of the scaffolds increased from 30% to 100%, the Young's modulus decreased from 26.2 ± 8.2 to 1.2 ± 0.1 MPa and the elongation at break increased from 40.7 ± 4.5% to 129.3 ± 19.4%, indicating increased elasticity and demonstrating the intrinsic elastic properties of the TE molecule.[12] The Young's modulus of the TE30 and TE50 scaffolds were ≈18 and 8 times higher, respectively, than a healthy human coronary artery, which has a Young's modulus of 1.5 MPa.[13] The Young's modulus of TE70 (1.3 ± 0.1 MPa) was similar to a human coronary artery. TE50 had the highest UTS of 8.0 ± 2.1 MPa among the electrospun TE-PGS scaffolds, possibly due to its fiber-reinforced matrix microstructure. TE30 has a similar matrix microstructure but demonstrated a reduced UTS of 4.3 ± 0.1 MPa which is likely due to a decreased TE fiber network density and heterogeneous morphology.

A creep test was performed over 500 min at a constant load of 0.1 MPa to examine scaffold viscoelasticity and evaluate mechanical stability. Stages of the creep test are marked on Figure 2F. After an initial elastic deformation due to loading at stage (1), TE100 experienced the greatest creep rate in both the creep stage (2) and the fast creep stage (3) compared to the other scaffolds, which showed similar creep rates. The creep rate of TE100 continued to rise during the rebound stage (4) whereas the other scaffolds experienced rebound. All scaffolds returned to their preloaded dimensions when the load was removed. A 1000 cycle tensile test at a force-ramp rate of 0.1 N min^{-1} was

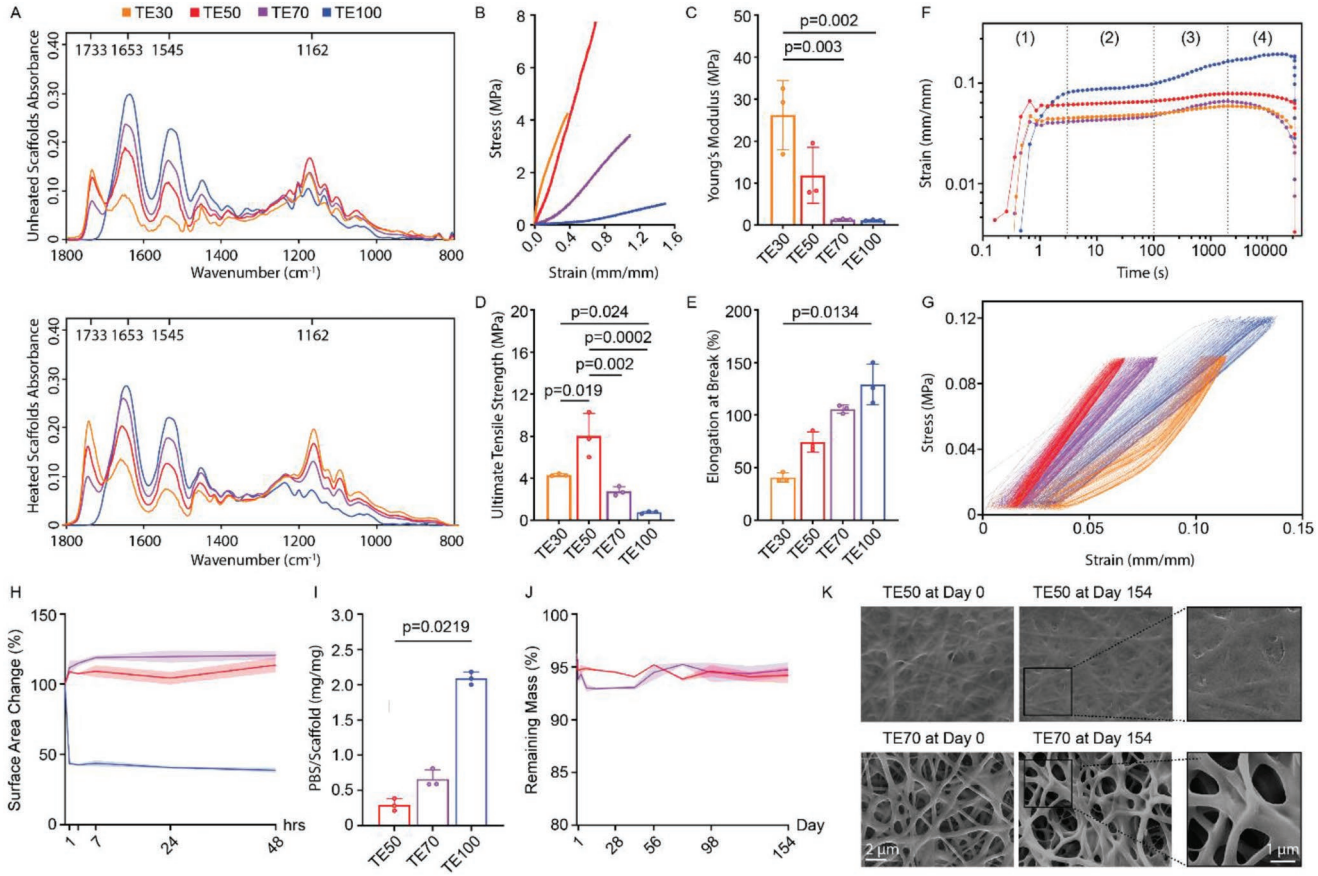

Figure 2. Characterization of electrospun TE-PGS scaffolds. A) FTIR-ATR spectrum of scaffolds showing no chemical changes after heat stabilization. B–G) Scaffold mechanical properties are shown in stress–strain curve (B), Young's modulus (C), ultimate tensile strength (D), elongation at break (E), creep test (F), and cyclic tensile test (not all cycles are shown) (G). H–K) The stability of the scaffolds was assessed through surface area changes (H), liquid uptake (I), mass degradation (J), and morphology changes (K) before and after submersion in PBS for 154 days. $n = 3$ for all quantitative experiments.

conducted to assess the performance of the scaffolds under a dynamic mechanical environment. The cyclic tensile test indicated that TE30 exhibits a nonlinear stress response with a low modulus at early strains and a higher modulus at greater strains whereas TE50, TE70, and TE100 were elastic with negligible hysteresis evident throughout the 1000 cycles (Figure 2G). These mechanical properties indicate that all TE-PGS scaffolds should be sufficient to withstand arterial blood pressure immediately following implantation. However, the defects and inhomogeneity generated during electrospinning of the TE30 scaffold (Figure 1D) poses a concern for fabrication consistency and likely resulted in its nonlinear stress–strain behavior. Therefore, TE30 was eliminated as a candidate scaffold.

2.3. Stability of Electrospun TE-PGS Scaffolds

Maintenance of both scaffold dimensions and structural integrity were assessed through submersion in phosphate-buffered saline (PBS) at the elevated, physiologically relevant temperature of 37 °C. 1 h after submersion, the surface areas of TE50 and TE70 had increased 8.7 ± 0.9% and 11.6 ± 4.3%, respectively (Figure 2H and Figure S2, Supporting Information). These changes corresponded to liquid retentions of 0.29 ± 0.07 mg PBS mg^{-1} for TE50 scaffolds and 0.66 ± 0.10 mg PBS mg^{-1} for TE70 scaffolds (Figure 2I). In contrast, the TE100 sample shrank rapidly, minutes after contacting PBS at 37 °C, and showed a 56.4 ± 0.9% reduction in surface area after 1 h. Despite shrinking, TE100 samples absorbed 2.10 ± 0.07 mg PBS mg^{-1}, which is 7 times that of TE50 scaffolds and 19 times that of TE70 scaffolds. Over 48 h, the dimensions of the TE50 and TE70 scaffolds gradually expanded and stabilized with final surface area increases of 13.6 ± 4.2% and 20.4 ± 2.4%, respectively. TE100 shrank 61.2 ± 1.5% from its original surface area over 48 h. This substantial dimensional change under physiological conditions rendered electrospun TE100 scaffolds unsuitable for vascular graft applications.

The long-term stability of TE50 and TE70 was evaluated over 154 days by observing mass changes following submersion in PBS. TE50 and TE70 lost 5% and 6% respectively of their initial mass during the first 24 h in PBS (Figure 2J), which was likely to correspond to the removal of non-cured PGS as no TE or TE degradation products were observed by sodium dodecylsulfate polyacrylamide gel electrophoresis analysis (Figure S3, Supporting Information). No further significant mass loss was observed over the 154 days, which indicates the scaffolds are

stable in vitro. Comparison of SEM images at day 0 and day 154 indicated there was no change in morphology for TE50 (Figure 2K). However, the fibers within TE70 appeared more wrinkled compared to the non-treated samples due to water uptake but remained fibrous and porous. No or minimal morphological changes in TE50 and TE70 confirms the long-term integrity of these scaffolds.

2.4. In Vitro Cytocompatibility and In Vivo Biocompatibility of TE-PGS Scaffolds

The in vitro cytocompatibility of TE50 and TE70 was assessed by culturing the scaffolds with human dermal fibroblasts (HDFs) for 7 days. A PGS scaffold was used as a control to illustrate the benefits of TE. HDFs could attach to and proliferate on TE50 and TE70 scaffolds but failed to attach to and proliferate on PGS scaffolds (**Figure 3**A). Assessment of HDF morphology on day 7 showed the presence of elongated actin fibers within most of the cells on TE50 and TE70 scaffolds (Figure 3B). SEM images captured a remaining HDF cultured on a PGS scaffold undergoing apoptosis, whereas multiple HDFs with elongated and flattened morphologies were observed on TE50 and TE70 scaffolds (Figure 3C). Furthermore, high-resolution SEM images showed interactions between HDFs and the electrospun TE-PGS scaffolds through extended filopodia, which may be a result of the fibrous nature of the electrospun scaffolds that mimic the ECM.

We then examined the in vivo biocompatibility of TE50 and TE70 scaffolds through subcutaneous implantation in mice with subsequent histological assessment at 14 and 28 days (Figure 3D). This allowed for fibrous capsule formation to be assessed over the time course. TE50 and TE70 scaffolds were surrounded by fibrous capsules that appeared to be thinner and contained fewer dense collagen fibers with a decreased total number of cells at day 14 and 28 compared to the PGS scaffolds (Figure 3E,F). No cell invasion was observed within either the TE50 or TE70 scaffolds. These observations indicate that the TE50 and TE70 scaffolds are tolerated subcutaneously, and that the addition of TE could reduce fibrosis. Biodegradable scaffolds do not generate a persistent fibrous capsule, rather the capsule becomes thinner and eventually disappears as the material degrades.[14] Here we see that the thickness of the fibrous capsule surrounding PGS at day 28 had significantly decreased from day 14, indicating its ongoing degradation. While the thickness of the fibrous capsule surrounding TE50 and TE70 had not changed at day 28 it is likely that a longer subcutaneous implantation study would elucidate the biodegradation profile of these scaffolds.

2.5. Interaction of TE-PGS Scaffolds with Vascular Cells

To assess the potential of TE-PGS scaffolds in vascular graft applications, we evaluated the ability of human umbilical vein endothelial cells (HUVECs) and human coronary artery smooth muscle cells (HCASMCs) to proliferate and express functional markers when cultured on them. Seeded HUVECs were able to attach and spread on TE50 and TE70 scaffolds with significant cell proliferation evident between day 1 and day 7 (Figure 3G). Cell numbers increased 11.5-fold and 9.3-fold over the 7 days on TE50 and TE70 scaffolds, respectively. By day 7, HUVECs cultured on these scaffolds had formed a near-complete monolayer with polygonal morphologies (Figure 3H). In contrast, HUVECs seeded onto PGS displayed a rounded morphology and failed to proliferate. Gene expression of functional endothelial cell markers was analyzed using RT-qPCR. This could not be performed on HUVECs cultured on the PGS scaffold as no cell growth was observed. Gene expression of *CDH5*, the encoding gene for the adherens junction protein vascular endothelial cadherin (VE-Cad), was significantly higher in HUVECs that had been cultured on TE70 for 7 days compared to cells cultured on the scaffold for 1 day (Figure 3I). No significant difference was observed in *CDH5* expression levels between cells cultured on TE50 for 1 or 7 days. Gene expression of *VWF*, the encoding gene for the clotting protein von Willebrand factor (vWF), increased significantly from day 1 to day 7 in HUVECs cultured on both TE-PGS scaffolds. Gene expression of *NOS3*, the encoding gene for the enzyme endothelial nitric oxide synthase (eNOS) that is involved in NO production, did not change significantly over time on either electrospun TE-PGS scaffolds. This lack of change in *NOS3* expression may be due to the use of a static culture method rather than dynamic culture methods[15] as eNOS expression in arterial ECs has been shown to be modulated by hemodynamic forces.[16] Immunofluorescence (IF) staining was used to confirm HUVEC expression of the three key functional markers for endothelium, VE-Cad, eNOS, and vWF, at the protein level on both of the TE-PGS scaffolds. All three proteins were present within the HUVEC monolayers after 7 days of culture on the scaffolds (Figure 3J). Specifically, VE-Cad was localized to the cell–cell boundaries and formed a continuous band around each cell, indicating the successful formation of an endothelial monolayer with adherens junctions at cell–cell interfaces. eNOS and vWF were observed scattered throughout the monolayer and their presence indicated that HUVECs cultured on TE-PGS scaffolds can produce NO and perform coagulation activities, respectively, which are necessary functions of the arterial endothelium.[17]

HCASMCs were cultured on the PGS and TE-PGS scaffolds for 7 or 14 days, and their morphology and function were also assessed through IF and RT-qPCR. Over 7 days, HCASMCs proliferated on TE-PGS scaffolds but did not significantly increase in number on PGS scaffolds (Figure 3G). F-actin staining revealed the morphology of the HCASMCs on the TE-PGS scaffolds changed from a rhomboid shape with cells spreading in random directions on day 1 to most cells aligning with an elongated spindle shape by day 14 (Figure 3H). HCASMCs cultured on PGS presented with a rounded morphology on day 1 with no cells present on the scaffold on day 14. To assess the phenotype of HCASMCs cultured on TE-PGS scaffolds for 14 days, RT-qPCR was used to determine the gene expression of *ACTA2* and *MYH11* (Figure 3K), which are the genes encoding for α-smooth muscle actin (α-SMA) and smooth muscle-myosin heavy chain (SM-MHC), respectively. The deposition of these proteins within the cell layer was assessed by IF (Figure 3L). Compared to gene expression at day 1, TE50 did not promote expression level changes in *ACTA2* or *MYH11* at day 14, whereas a significant increase in *ACTA2* expression was seen

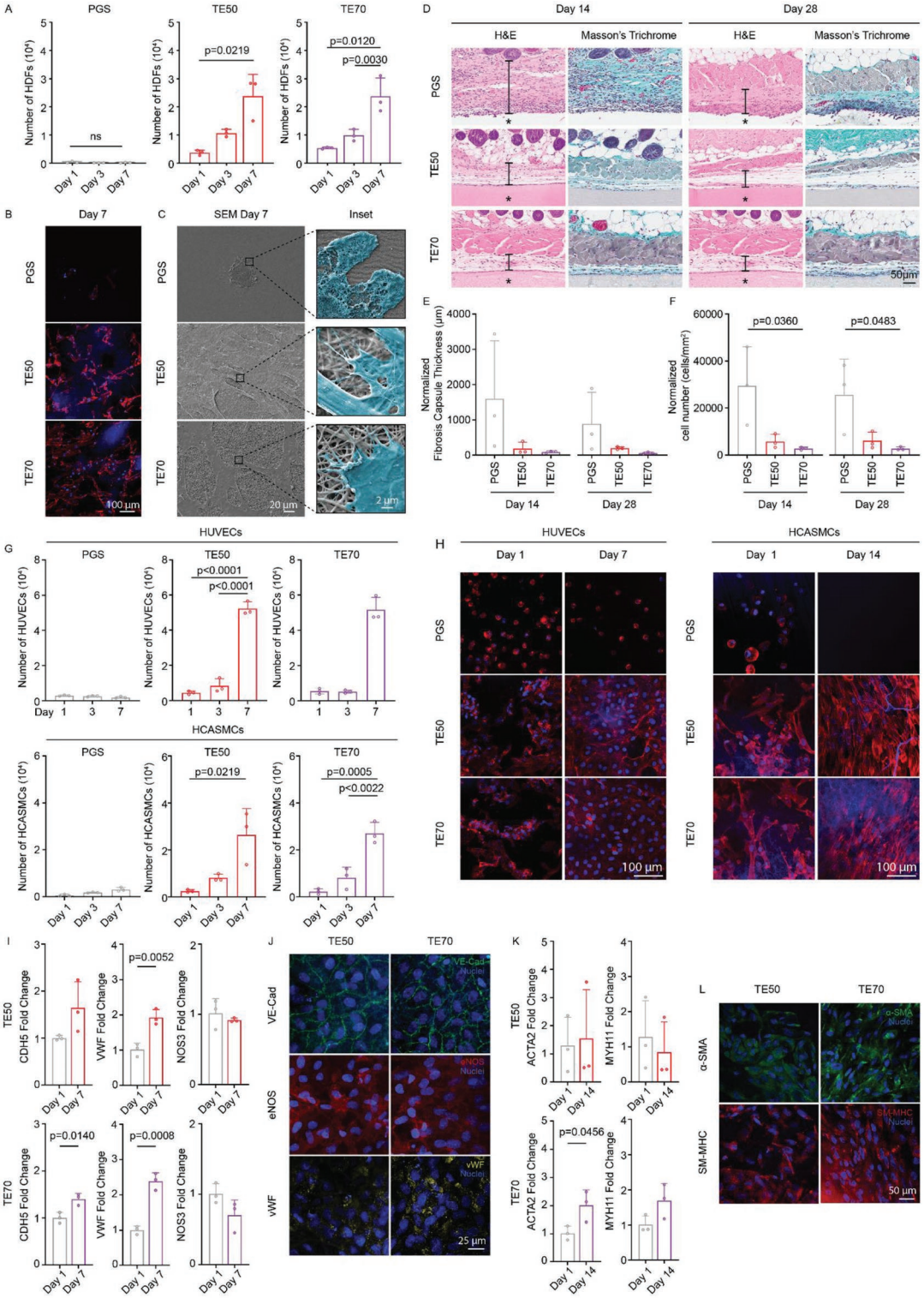

Figure 3. In vitro and in vivo evaluation of the biocompatibility of TE-PGS scaffolds. A) Human dermal fibroblast (HDF) proliferation on PGS, TE50, and TE70. B,C) Morphological assessment of cultured HDFs on scaffolds through immunofluorescence staining of F-actin (red) and nuclei (blue) (B) and SEM with cells false-colored blue to highlight their interactions with the underlying scaffolds (C). D) Histological assessment of scaffolds subcutaneously implanted in mice for 14 and 28 days using H&E and Masson's trichrome staining. E,F) H&E staining was used to assess fibrous capsule thickness (E) and the total number of cells surrounding the scaffolds (F), both normalized to the scaffold area. G–K) Interaction of TE-PGS scaffolds with vascular cells. G) Proliferation and H) morphology (F-actin in red and nuclei in blue) of human umbilical vein endothelial cells (HUVECs) and human coronary artery smooth muscle cell (HCASMCs). I) Relative gene expression of CDH5, VWF, and NOS3. J) Functional marker expression of VE-Cad (green), eNOS (red), and vWF (yellow) with nuclei (blue). K) Relative gene expressions of ACTA2 and MYH11. L) functional marker expression of α-SMA (green) and SM-MHC (red) with nuclei (blue). $n = 3$ for all quantitative experiments.

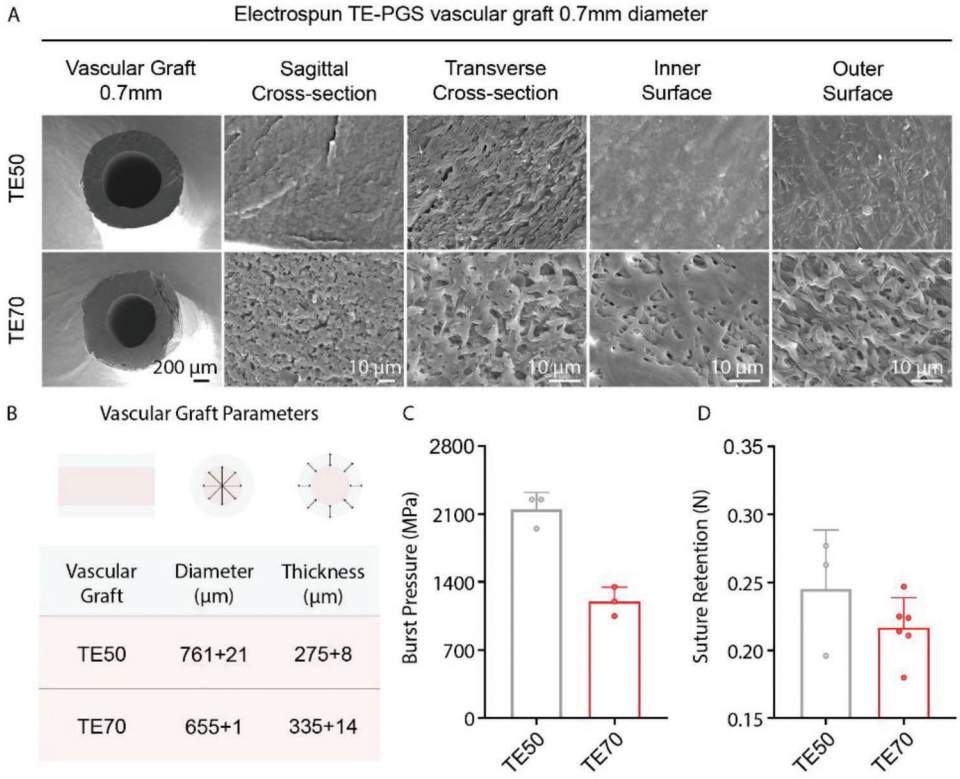

Figure 4. Morphological, geometrical, and mechanical characterization of fabricated TE-PGS vascular grafts. A) SEM showing morphologies of TE50 and TE70 at parallel and perpendicular cross-sections, inner surface, and outer surface. B) Diameter and thickness of TE50 and TE70. C,D) Mechanical properties of TE50 and TE70 including burst pressure (C) and suture retention (D). $n = 3–6$ for all quantitative experiments.

on TE70. No change in *MYH11* expression was seen on TE70. IF indicated that HCASMCs cultured on both scaffolds expressed both α-SMA and SM-MHC. These results indicate that TE-PGS scaffolds supported the proliferation of cultured HCASMCs and their differentiation into a contractile phenotype.[18]

2.6. Fabrication of TE-PGS Vascular Grafts and Pre-Implantation Assessments

Tubular vascular grafts, with various diameters (0.7, 1, and 1.5 mm) and wall thicknesses, were successfully fabricated by electrospinning different volumes of blended TE-PGS solutions (0.5, 0.7, and 1 mL) onto assorted sized mandrels (Figure S4, Supporting information). The morphologies of the fabricated TE-PGS vascular grafts were examined by SEM (**Figure 4**A) and the diameter and wall thickness of the grafts are shown in Figure 4B. TE50 grafts were non-porous and appeared fiber-reinforced. TE70 grafts were fibrous and contained some pores but they were not interconnected. Contact with the mandrel on the interior of the graft resulted in a flatter surface with more fused fibers compared to the outer surface.

The grafts fabricated from 0.7 mL TE-PGS blend solutions were subjected to mechanical tests, including burst pressure, suture retention, and kink angle analysis. The average burst pressures of TE50 and TE70 grafts were 2150 ± 173 and 1200 ± 150 mmHg, respectively (Figure 4C). The burst pressures of both grafts were higher than the physiological pressures of 90 to 115 mmHg reported in wild type mice,[19] 80 to 120 mmHg found in healthy human subjects and 90 to, in rare cases, greater than 250 mmHg observed in hypertensive patients.[20]The burst pressure of a typical mouse aorta is not available as the multiple branches cannot be stably pressurized during testing.[21] However, both TE50 and TE70 grafts have burst pressures lower than that reported for the rat aorta of 3415 ± 529 mmHg.[22] The suture retention values for TE50 and TE70 grafts were determined to be 0.25 ± 0.04 and 0.22 ± 0.02 N, respectively (Figure 4D), which were higher than those of mouse aorta (0.10 ± 0.04 N)[21] and cast PGS vascular grafts (0.11 ± 0.0087 N),[22] and lower than the break force of 7–0 polypropylene sutures (3.7 N, Ethicon) that are commonly used in humans.[23] These data indicate that the fabricated TE-PGS grafts are suturable with adequate suture retention properties.

We also assessed the thrombogenicity of the scaffolds before implantation. Adhesion of heparinized (0.5 U heparin per mL) whole blood to 316L stainless steel—a common component of commercial stents,[24] and PGS, TE50, TE70, and TE100 was measured over 10, 30, and 60 min with shaking at 37 °C (Figure S5, Supporting Information). Whole blood consists of red blood cells (RBCs), plasma, and platelets that can form a thrombus. At 10 min, stainless steel, PGS, and TE50 showed similar amounts of adhered RBCs and platelets without the formation of a fibrin matrix. In contrast, a fibrin matrix had formed on TE70. TE100 showed obvious thrombus formation indicated by a densely packed fibrin matrix with trapped RBCs. At 30 min, stainless steel and PGS showed a similar number

of adhered RBCs and platelets. Aggregations of platelets and RBCs with a fibrin matrix could be seen on both TE50 and TE70. At 60 min, scattered aggregations of platelets and RBCs with a fibrin matrix were present on stainless steel, TE50, and TE70 while multiple layers of thrombus had formed on TE100. The lowest number of aggregated platelets and RBCs and no obvious fibrin matrix formation was observed on PGS. Based on these results, TE70 displayed higher potential for thrombosis compared to TE50 and was excluded from animal studies. We recognize however that the thrombogenicity of TE50 is not ideal compared to autologous grafts, which do not cause thrombosis due to the presence of an intact endothelium. Future iterations of the TE50 graft could be improved by precoating with heparin to inhibit blood clotting.[22]

2.7. Implantation Study

TE50 vascular grafts were evaluated as interpositional implants in the infrarenal abdominal aorta of beige mice over an 8 month period. Ultrasound monitoring indicated that TE50 grafts with an initial diameter of 0.7 mm continued to dilate until 18 weeks before gradually stabilizing with a final diameter of 1.4 ± 0.2 mm at 8 months (Figure S6A,B, Supporting Information). No localized aneurysms were detected throughout the study. Over the 8 months the pulsatility of the TE50 grafts increased from 2.1 ± 0.5% to a maximum of 4.8 ± 1.1% at 13 weeks before dropping to 1.8 ± 0.7% by 8 months likely due to the significantly increased graft diameter (Figure S6C, Supporting Information). Graft degradation and tissue remodeling were anticipated to occur rapidly after implantation due to the reported degradation profile of PGS,[9,22] allowing for the formation of a neoartery. H&E staining (**Figure 5**A) of explanted grafts at 8 weeks indicated that two distinct cellularized regions had formed: an ECM-dense inner zone and a looser outer zone. By 8 months the TE50 graft was no longer evident but the distinct regions had persisted and the neoartery appeared more organized. The rapid degradation of PGS following implantation is likely to have contributed to the initial dilation rate (0–18 weeks), while remodeling of the graft through cellular infiltration and ECM deposition over 18 weeks and beyond resulted in the formation of a neoartery with adequate mechanical strength to resist further dilation. Over time, the average wall thickness of the neoartery decreased from 245.8 ± 32.4 μm at 8 weeks to 189.6 ± 51.3 μm at 8 months, similar to that of mouse AA (176.0 ± 43.4 μm).

To further investigate the process of graft degradation, immunofluorescence staining was used to detect the presence of macrophages and their subphenotypes, given their crucial role in implant removal and remodeling (Figure 5B). Staining for F4/80$^+$, a general marker for murine blood-circulating monocytes and macrophages,[25] revealed that the average area of F4/80$^+$ staining within the graft dropped significantly from 21.7 ± 5.4% at 8 weeks to 4.5 ± 1.2% at 8 months, signaling the resolution of inflammation and remodeling (Figure 5C). This also corresponded to a significant reduction in iNOS$^+$ staining, a marker of pro-inflammatory M1 macrophages from 6.0 ± 1.6% at 8 weeks to 2.0 ± 1.7% at 8 months and CD206$^+$ staining, a marker of anti-inflammatory M2 macrophages from 7.6 ± 2.6% at 8 weeks to 1.7 ± 0.7% at 8 months (Figure 5D,E). The iNOS$^+$/CD206$^+$ ratio did not change significantly between 8 weeks and 8 months (Figure 5F). Interestingly, we observed differences in the spatial distribution of the macrophages possibly due to the barrier-like surface the non-porous TE50 graft presented. More iNOS$^+$ M1 and CD206$^+$ M2 macrophages had accumulated in the adventitia region of the neoartery compared to the intima-media region at 8 weeks (Figure 5G). In the adventitia region, M1 macrophages were present in the area immediately next to the implant while M2 macrophages occupied the entire region and likely facilitated tissue remodeling.[26] These adventitial macrophages could have migrated from surrounding connective or adipose tissue or adjacent tissue via the anastomosis site.[27] The average fraction of M1 and M2 macrophages in the adventitia region substantially decreased by 8 months (Figure 5H) in accordance with the removal of TE50. In contrast, the intima-media region contained a small fraction of M1 and M2 macrophages at 8 weeks that did not change by 8 months. These macrophages were likely either derived from blood-circulating monocytes or had migrated from adjacent tissue via the anastomoses.[27c,28]

We investigated the distribution of elastin, collagen, CD31$^+$ endothelial cells, α-SMA$^+$, and smoothelin$^+$ SMCs within the regenerated neoartery at 8 weeks and 8 months compared to mouse AA (**Figure 6**). Verhoeff–Van Gieson (VVG) staining revealed that 8 weeks post-implantation, long, continuous, circumferentially-aligned EL had been generated within the intima-media region of the neoartery, which were still present at 8 months (Figure 6A). The EL were organized with distinct morphologies that contrasted with the disorganized VVG staining that was seen throughout the graft prior to implantation (Figure S7, Supporting Information). The elastin fraction of the neoartery was 13.9 ± 4.9% at 8 weeks and 21.4 ± 5.6% at 8 months which were both similar to the elastin content of mouse AA (14.8 ± 4.9%) (Figure 6E). Picrosirius red (PSR) staining indicated that loose and thin type I and III collagen fibers that were deposited in the adventitia of the neoartery by 8 weeks became thicker and denser and acquired a basket weave morphology approaching that in the mouse AA by 8 months (Figure 6B). Early stage collagen deposition was likely initiated by adventitial fibroblasts under the stimulation of M2 macrophages with secreted factors such as TGF-β1,[29] while later collagen remodeling was possibly due to the balanced activities of matrix metalloproteinases (MMPs) and tissue inhibitors of MMPs modulated by cross-talk between adventitial fibroblasts and M2 macrophages.[30] Quantification of polarized PSR staining revealed that the neoartery contained a total collagen fraction of 9.4 ± 2.2% at 8 weeks and 13.0 ± 5.5% at 8 months, which approached that found in mouse AA (16.4 ± 4.7%) (Figure 6F). By 8 weeks CD31$^+$ endothelial cells completely covered the lumen of the neoartery and this newly formed endothelium remained intact at 8 months (Figure 6C). Staining for α-SMA$^+$ and smoothelin$^+$ SMCs showed these cells were primarily located in the intima-media region of the neoartery at both 8 weeks and 8 months (Figure 6D,E) and were present at similar levels to the mouse AA (Figure 6H,I).

We then further characterized the regenerated EL within the intima-media region of the neoartery and compared these to the EL in the native mouse AA (**Figure 7** and Videos SV1 and

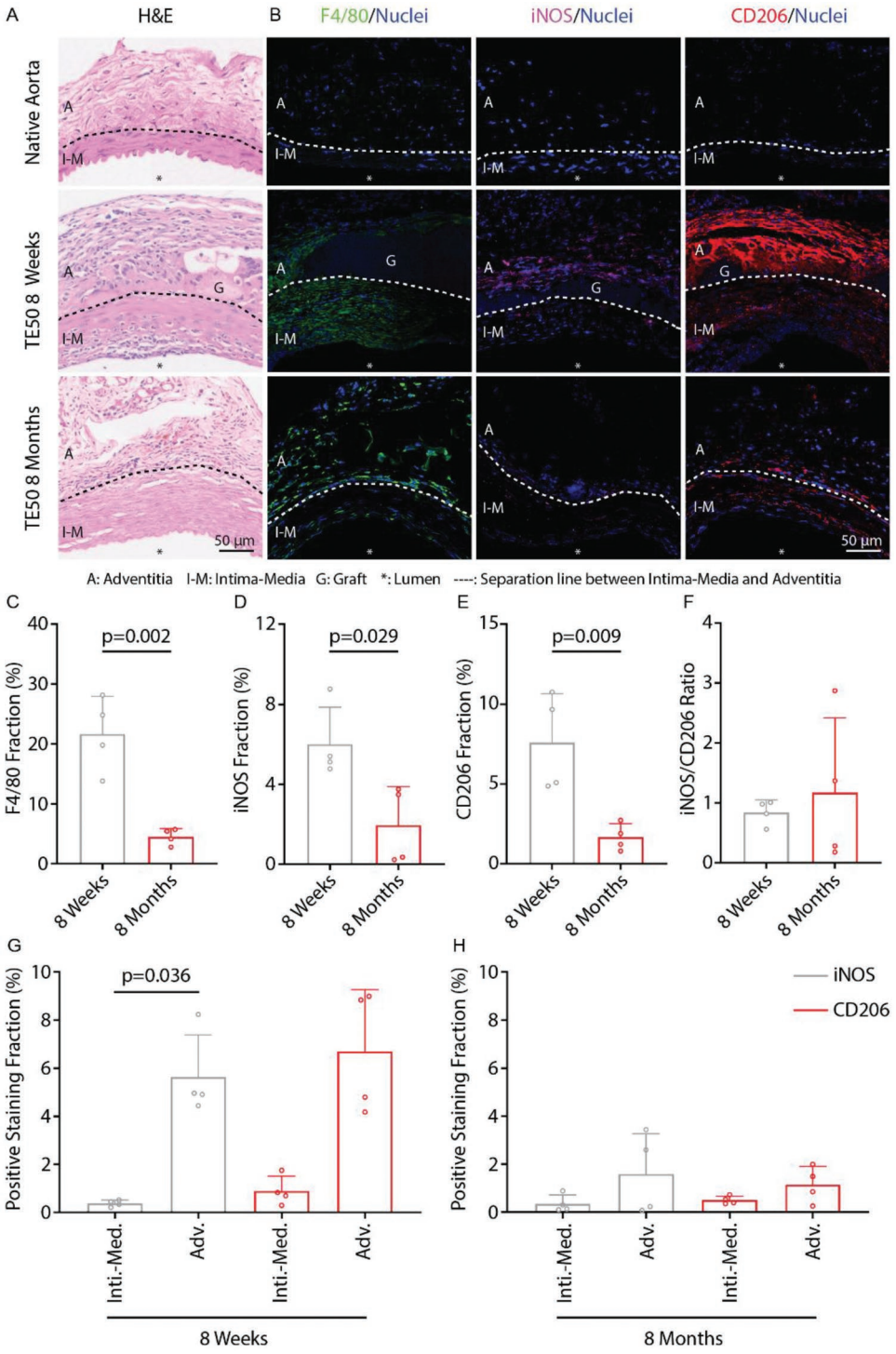

Figure 5. H&E staining and macrophage response to implanted TE50 at 8 weeks and 8 months compared to mouse abdominal aorta. A) H&E staining with intima-media (I-M), adventitia (A) and graft (G) indicated. B) Immunofluorescence staining of F4/80 (green), iNOS (magenta), and CD206 (red) with nuclei (blue). C–G) Quantitative analyses of F4/80$^+$ fraction (C), iNOS$^+$ fraction (D), CD206$^+$ fraction (E), iNOS$^+$ to CD206$^+$ ratio (F), and G,H) iNOS$^+$ and CD206$^+$ distribution between intima-media (Inti.-Med.) and adventitia (Adv.) regions at 8 weeks (G) and 8 months (H). $n = 4$ for all quantitative experiments.

SV2, Supporting Information). Both VVG staining (Figure 7A) and elastin autofluorescence (Figure 7B) showed the presence of continuous, wavy EL. These regenerated EL had an average thickness of 1.6 ± 0.4 μm at 8 weeks and 1.8 ± 0.1 μm at 8 months, which was about half the thickness of the EL (3.1 ± 0.7 μm) in mouse AA (Figure 7G). However, the number of EL in the neoartery was on average 8.5 ± 1.4 and 8.7 ± 1.2 at 8 weeks and 8 months, respectively, which was approximately

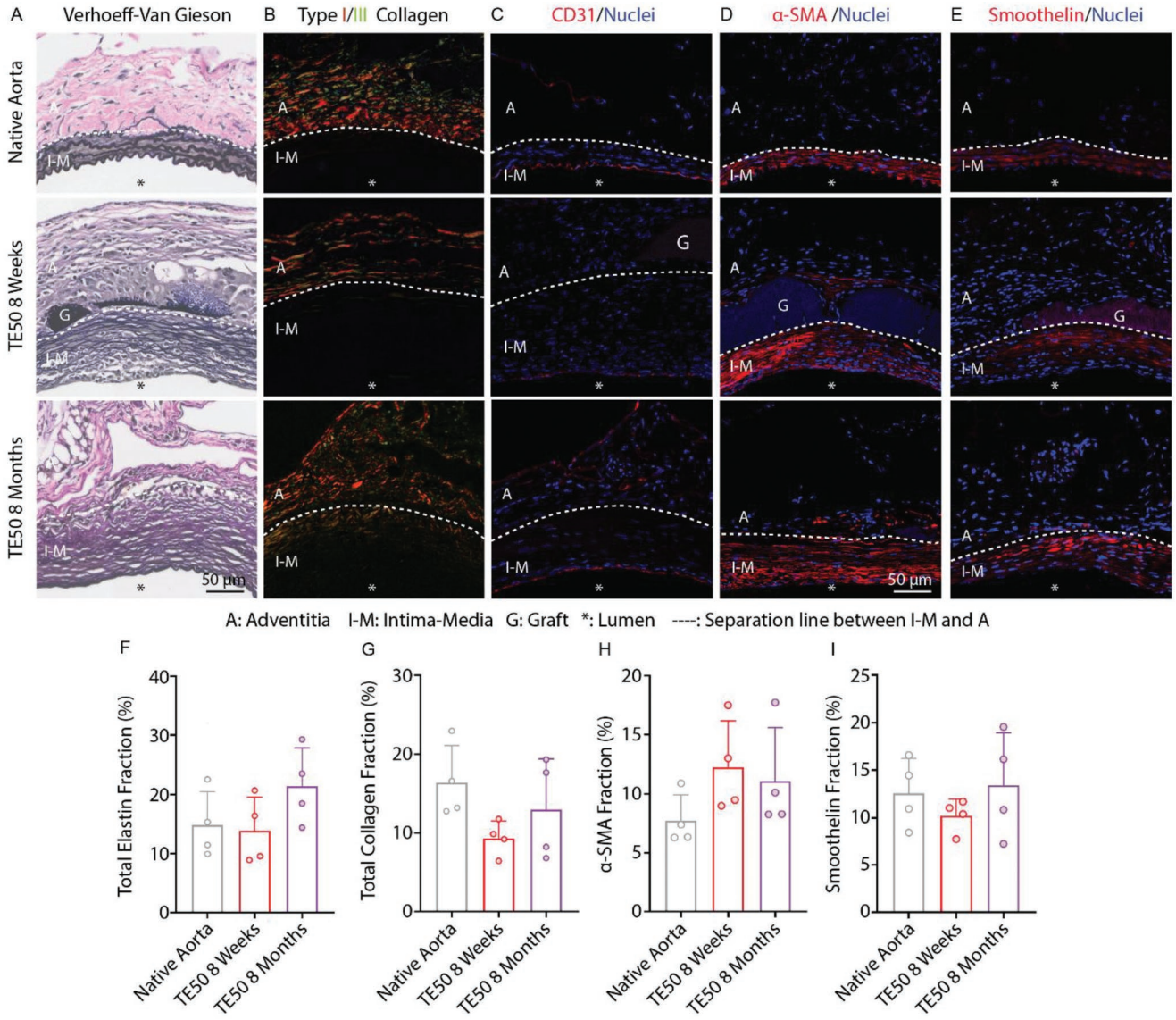

Figure 6. Extracellular matrix and cellular components of explanted TE50 grafts at 8 weeks and 8 months compared to mouse abdominal aorta. A,B) Representative histology images of Verhoeff–Van Gieson staining showing elastin (black) (A) and Picrosirius Red staining under polarized light showing type I collagen (red) and type III collagen (green) (B). C–E) Representative images of immunofluorescence (IF)-stained CD31$^+$ endothelial cells (red) (C), α-SMA$^+$ (red) cells (D), and smoothelin$^+$ (red) (E) smooth muscle cells with nuclei (blue). F–I) Quantification of total elastin fraction (F), total collagen fraction (G), α-SMA fraction (H), and smoothelin fraction (I) from histology and IF staining. $n = 4$ for all quantitative experiments.

twice the number of EL (3.9 ± 0.1) observed in the mouse AA (Figure 7H). Throughout the region, α-SMA$^+$ and smoothelin$^+$ SMCs were circumferentially aligned in layers between the EL (Figure 7D and E). SMCs are responsible for the production of amorphous elastin and elastic fibers,[31] and we assume these SMCs contributed to the accumulation and remodeling of elastin into EL in this study. EL in the neoartery were also surrounded by fibrillin-1 (Figure 7C), which is a crucial component in elastic fiber assembly and an indicator of de novo elastogenesis.[32] The presence of aligned α-SMA$^+$ and smoothelin$^+$ SMCs as well as fibrillin-1 sandwiching the regenerated EL within the intima-media demonstrates a high level of EL organization and structural similarity to the mouse AA. Furthermore, we also observed regeneration of an IEL in the neoartery which had a thickness and continuity comparable to the IEL in the mouse AA. Arterial SMCs and ECs are both individually capable of generating an IEL in mice AA.[33] However, it is likely that they participate together in the IEL morphogenesis process, which corresponds to the presence of both α-SMA$^+$ and smoothelin$^+$ SMCs and CD31$^+$ ECs in close association with the regenerated IEL in the neoartery (Figure 7F).

The results shown here demonstrate for the first time that we are aware of, the generation of a neoartery, from an implanted vascular graft, that recapitulates the native artery with respect to the content and spatial distribution of both collagen and organized EL. We propose a model of graft regeneration based on the non-porous nature of the TE50 grafts (**Figure 8**). Traditionally, the use of porous grafts in vascular settings[7b,c,22,34] has

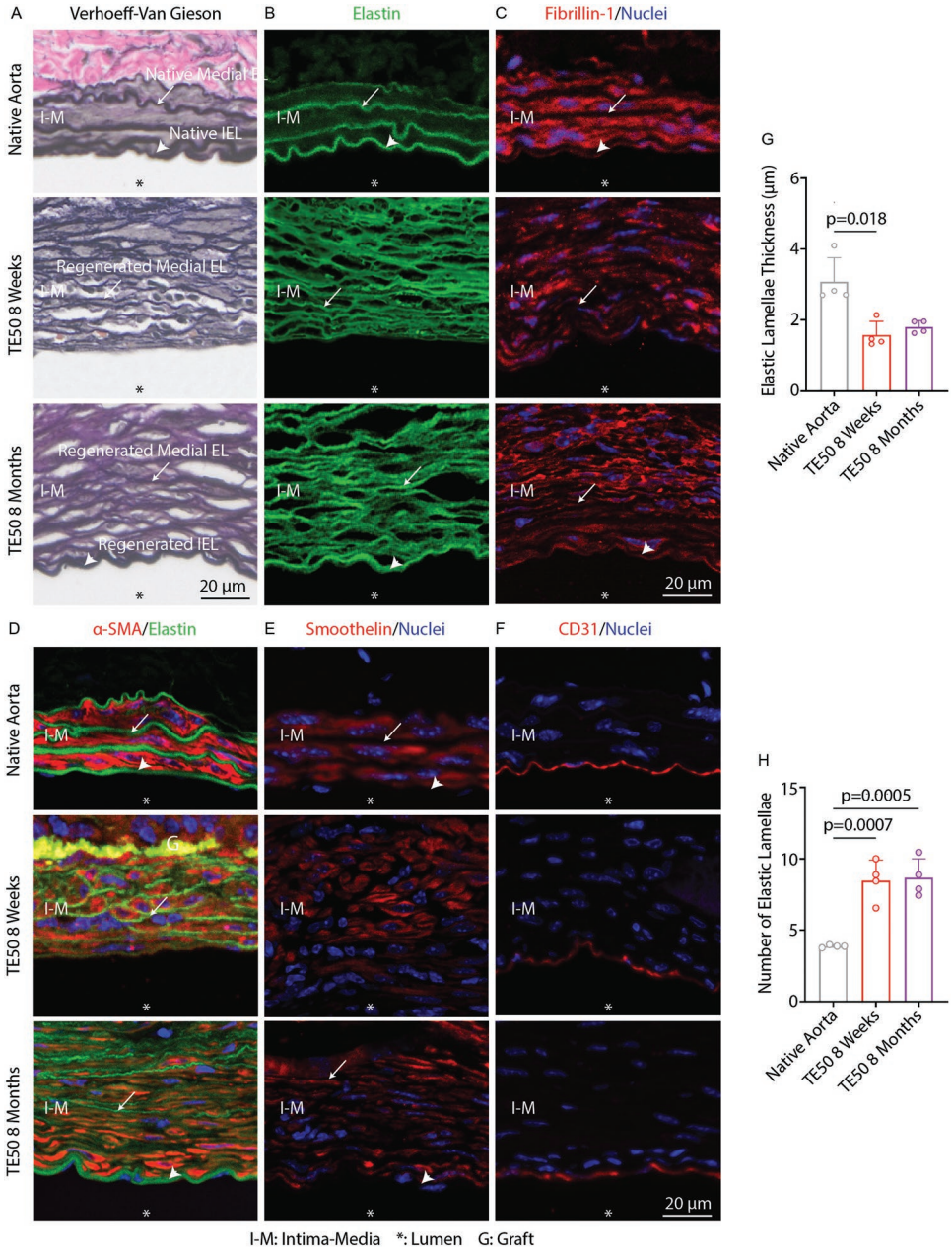

Figure 7. De novo regeneration of elastic lamellae (EL) within the intima-media region of the TE50 graft. A) Representative images of A)Verhoeff–Van Gieson staining showing organized EL (black) and B) autofluorescence of EL in green. C–F) Representative images of immunofluorescence stained fibrillin-1(red) (C), α-SMA (red) (D), smoothelin (red) (E), and CD31 (red) (F) associated with the regenerated EL and cell nuclei (blue). Quantification of G) EL thickness sand H) EL number. $n = 4$ for all quantitative experiments.

permitted the uncontrolled migration and infiltration of fibroblasts and arterial SMCs from adjacent native tissue into the implanted graft to synthesize ECM, in chaotic competition with infiltrating phagocyte-like macrophages that attempt to degrade the graft. This results in the random deposition of collagen and elastin within the graft pores. We propose that the graft then serves as a physical barrier that prevents the deposited amorphous elastin from connecting and organizing into EL. This contrasts with EL morphogenesis during the gestational and postnatal stages where EL are generated in between circumferentially aligned layers of SMCs.[31a] We suggest the solid, fiber-reinforced TE50 grafts prohibit chaotic cell infiltration and that their degradation is executed through surface erosion and phagocytosis rather than bulk degradation.[9] This allows tissue-resident cell accumulation on both the luminal and outer surface of the graft. Soon after implantation, the luminal surface becomes populated with migrating arterial SMCs and ECs to form an intima-media, nurtured by sustained release of TE from the graft. ECs may also be differentiated from circulating monocytes.[35] The ECs quickly establish an endothelium which remains intact to prevent late-stage thrombosis, while the SMCs accumulate and produce amorphous elastin and fragmented

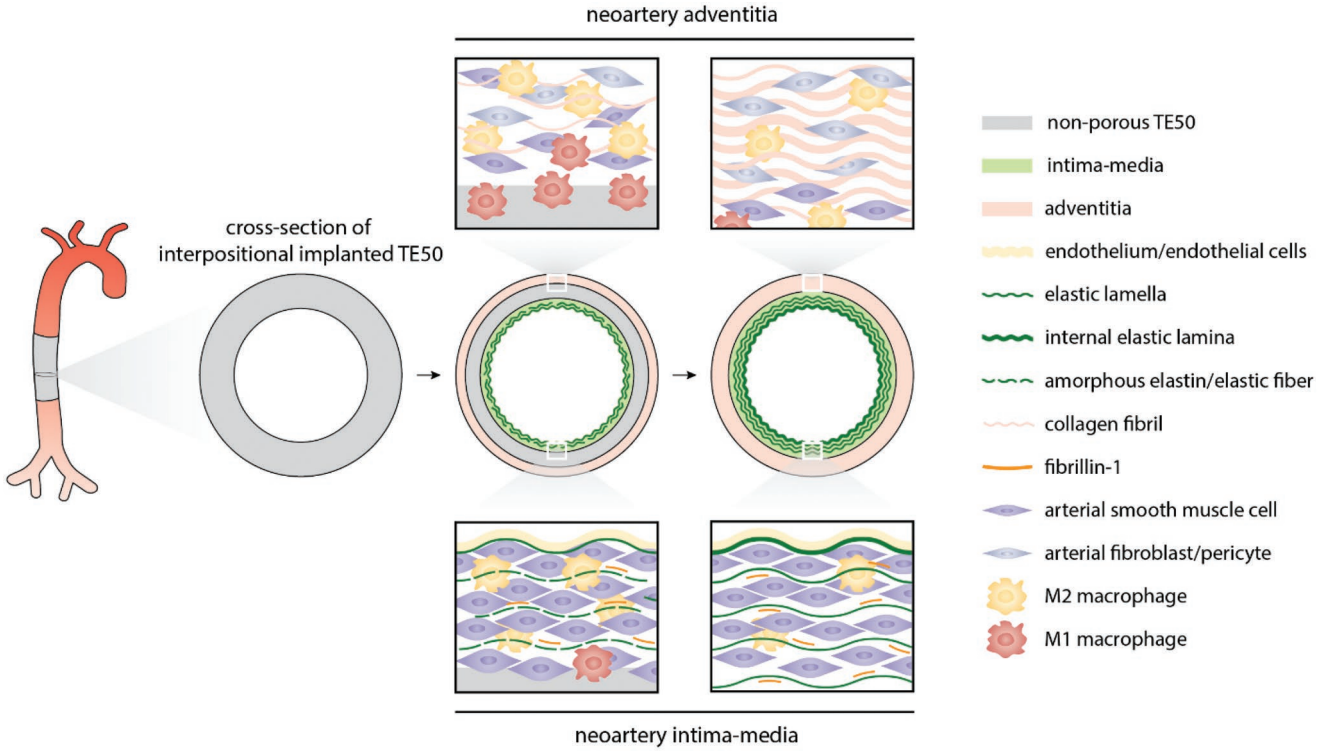

Figure 8. Proposed remodeling of TE50. After implantation, the non-porous TE50 vascular graft allows migration of arterial smooth muscle cells (SMCs) from adjacent tissue to form intima-media with a circumferential aligned and layered structure. TE is gradually released from the graft. Amorphous elastin and elastin fibers are produced and assembled to form elastic lamellae, possibly with the help of M2 macrophages. The internal elastic lamellae are formed at a later stage through the joined effort of SMCs and endothelial cells. The outer surface encounters both phagocytosis activities from M1 macrophages as well as the deposition and remodeling of collagen fibrils by an interplay of arterial SMCs, fibroblasts, pericytes, and M2 macrophages to form adventitia. Upon complete degradation of TE50, the adventitia meets intima-media to form the neoartery with spatial and microstructural features that resemble the native artery.

elastin fibers, which are then connected to form continuous EL. During this time, the newly formed endothelium also contributes to the production of organized elastin at the lumen interface along with the SMCs, gradually forming a thick IEL. The outer surface of the graft experiences most of the phagocytosis activities dominated by M1 macrophages. Fibroblast attachment and proliferation on this surface leads to the deposition of collagen fibrils, which gradually increase the tensile strength of the neoartery over time. M2 macrophages within the adventitia region continue to remodel collagen until its maturation. After the graft completely degrades, macrophage activities diminish, leaving a dense collagenous adventitia adjacent to an intima-media with alternatively sandwiched SMC layers and EL that resemble the native artery.

Despite the formation of a structurally appropriate neoartery the TE50 graft dilation and pulsatility data gathered over 8 months indicated a potential mismatch between the mechanical properties of the native artery and the regenerating graft. Dilation is known to reduce blood flow velocity and generate turbulence, which may limit the durability of the TE50 graft and should be prevented in future studies. This dilation of TE50 could be limited either by chemically modifying PGS[7b] to slow graft degradation or by reinforcing the graft through the addition of an outer sheath layer made from materials previously reported to facilitate collagen production.[7c] The mouse AA and neoarteries regenerated from TE50 grafts comprised similar fractions of elastin and SMCs, as well as a typical endothelium layer, but significantly lower amounts of collagen. It is likely that limited generation of collagen in the graft adventitia was the main contributing factor to graft dilation over time, with the loss of mechanical strength due to the rapid degradation of the original graft not compensated for by adequate collagen deposition. The dilation that the TE50 grafts experienced differs from that seen in aortic aneurysm, which is associated with an increase in collagen content as a response to selective elastin degradation.[36] Here EL generation occurred at an early stage, but limited collagen regeneration compromised the graft and led to early dilation. This indicates that early and balanced production of both organized elastin and collagen is required for the formation of a mechanically viable neoartery. Various groups have reported the generation of appropriate collagen types and amounts within their vascular graft prototypes and similar strategies could be adopted to improve the TE50 graft.[7b,c,22,37]

The de novo production of organized EL in the intima-media has been identified as the missing element in biodegradable vascular graft regeneration.[5,7a] Most elastogenesis is classically restricted to late fetal and early neonatal periods,[38] with limited elastin synthesis in adulthood that is in response to the loss of elastin due to injury or disease.[39] In blood vessels, elastin is an extremely durable insoluble protein and mature elastic fibers generally persist for the lifespan.[40]

We emphasize that in previous vascular graft implantation studies that have reported the synthesis of elastin, their elastin was amorphous and spatially distributed throughout the entire grafted region[22,37,41] or close to the lumen.[7b] Here, in contrast, we report the formation of mature, long, and continuous EL localized to the TE50 neoartery as early as 8 weeks after implantation and the development of an IEL, similar to the mouse AA IEL, by 8 months. To our knowledge, this is the first time the rapid de novo generation of elastin with such a degree of organization has been reported in a synthetic vascular graft. We note that the characteristics of the regenerated EL in the TE50 neoartery, including their thickness and numbers, show similarities to mice hemizygous for elastin , that is, $ELN^{+/-}$ mice.[42] $ELN^{+/-}$ mice have a normal lifespan despite showing significant hypertension.[43] The large blood vessels in $ELN^{+/-}$ mice show morphological changes in their deposited elastin compared to wild-type $ELN^{+/+}$ mice, including a 35% increase in the number of EL,[42a] a decrease in the distance between EL,[42b] and a roughly 50% reduction in lamellae thickness.[42b] Similarly, humans with ELN hemizygosity are reported to compensate for the reduction of ELN expression by developing a 250% increase in the number of EL.[42a] In support of this comparison, in the TE50 neoartery we saw a 220% increase in EL number, a 48.4% decrease in EL thickness and a decrease in the distance between EL.

TE is the monomer building block of elastin, elastic fibers, and EL in the artery.[44] TE50 is a non-porous PGS-based vascular graft that contains heat-stabilized human recombinant TE, which can release TE monomer and TE-based species during graft maturation.[11] As elastogenesis occurs when TE is supplied to fibroblasts in vitro,[45] we speculate that SMCs responded in a similar manner such that TE released from the TE50 graft promoted elastin production.

3. Conclusion

We have fabricated electrospun TE-PGS scaffolds with a spectrum of 3D microstructures. The scaffolds were mechanically robust, stable, and biocompatible as candidate materials for constructing off-the-shelf vascular grafts. TE50 and TE70 each supported HUVEC and HCASMC proliferation, and functional artery-related protein expression. TE50 was chosen for implantation in mouse AA as it was the least prone to thrombosis. The non-porous TE50 acted as a framework to stimulate distinctive regeneration profiles in the intima-media and the adventitia. By 8 months, the graft had completely degraded, forming a neoartery. The adventitia contained mature collagen. The intima-media contained organized EL that were sandwiched by circumferentially-aligned spindle-shaped α-SMA^+ and smoothelin$^+$ SMCs as early as 8 weeks. An IEL similar to that in mouse AA was formed by 8 months. Overall, we have shown the potential of TE50 as a functional vascular graft and presented a new class of material with the capacity to achieve complete arterial regeneration.

4. Experimental Section

The experimental details are provided in the Supporting Information.

Supporting Information

Supporting Information is available from the Wiley Online Library or from the author.

Acknowledgements

Z.W., H.V., and L.L. acknowledge an Australian Commonwealth Government Research Training Program Tuition Fee Offset and Z.W. and H.V. acknowledge an Australian Commonwealth Government Research Stipend Scholarship. A.S.W. acknowledges funding from the National Health and Medical Research Council. A.S.W. thanks Dr. Yadong Wang for encouraging the use of PGS. The authors acknowledge the technical and scientific assistance of Sydney Microscopy & Microanalysis, the University of Sydney node of Microscopy Australia and Sydney Analytical, a core research facility at The University of Sydney. All animal experiments and procedures were approved by Sydney Local Health District Animal Welfare Committee (AWC No. 2013/019D) under the Australian National Health and Medical Research Council guidelines for animal experimentation.

Open access publishing facilitated by The University of Sydney, as part of the Wiley - The University of Sydney agreement via the Council of Australian University Librarians.

Conflict of Interest

The authors declare no conflict of interest.

Data Availability Statement

The data that support the findings of this study are available from the corresponding author upon reasonable request.

Keywords

elastic lamellae, elastin, internal elastic lamina, polyglycerol sebacate, regenerative medicine, tissue engineering, tropoelastin, vascular grafts

Received: June 20, 2022
Revised: August 24, 2022
Published online: October 17, 2022

[1] P. Libby, *Sci. Am.* **2002**, *286*, 46.
[2] S. Pashneh-Tala, S. MacNeil, F. Claeyssens, *Tissue Eng., Part B* **2016**, *22*, 68.
[3] Y. Roina, F. Auber, D. Hocquet, G. Herlem, *Mater. Today Chem.* **2021**, *20*, 100412.
[4] Z. Wang, S. M. Mithieux, A. S. Weiss, *Adv. Healthcare Mater.* **2019**, *8*, 1900742.
[5] Z. Wang, L. Liu, S. M. Mithieux, A. S. Weiss, *Trends Biotechnol.* **2020**, *39*, 505.
[6] a) M. Lannoy, S. Slove, M.-P. Jacob, *Pathol. Biol.* **2014**, *62*, 79; b) X. Yu, R. Turcotte, F. Seta, Y. Zhang, *J. R. Soc., Interface* **2018**, *15*, 20180492.
[7] a) A. Patel, B. Fine, M. Sandig, K. Mequanint, *Cardiovasc. Res.* **2006**, *71*, 40; b) J. Fu, X. Ding, C. E. Stowell, Y.-L. Wu, Y. Wang, *Biomaterials* **2020**, *257*, 120251; c) J. Fu, M. Wang, I. De Vlaminck, Y. Wang, *Small* **2020**, *16*, 2004133.
[8] a) M. Koens, A. Krasznai, A. Hanssen, T. Hendriks, R. Praster, W. Daamen, J. Van Der Vliet, T. Van Kuppevelt, *Organogenesis* **2015**,

11, 105; b) M. J. McClure, D. G. Simpson, G. L. Bowlin, *J. Mech. Behav. Biomed. Mater.* **2012**, *10*, 48.
[9] Y. Wang, G. A. Ameer, B. J. Sheppard, R. Langer, *Nat. Biotechnol.* **2002**, *20*, 602.
[10] L. Vogt, F. Ruther, S. Salehi, A. R. Boccaccini, *Adv. Healthcare Mater.* **2021**, *10*, 2002026.
[11] S. M. Mithieux, B. Aghaei-Ghareh-Bolagh, L. Yan, K. V. Kuppan, Y. Wang, F. Garces-Suarez, Z. Li, P. K. Maitz, E. A. Carter, C. Limantoro, W. Chrzanowski, D. Cookson, A. Riboldi-Tunnicliffe, C. Baldock, K. Ohgo, K. K. Kumashiro, G. Edwards, A. S. Weiss, *Adv. Healthcare Mater.* **2018**, *7*, 1701206.
[12] J. Holst, S. Watson, M. S. Lord, S. S. Eamegdool, D. V. Bax, L. B. Nivison-Smith, A. Kondyurin, L. Ma, A. F. Oberhauser, A. S. Weiss, J. E. Rasko, *Nat. Biotechnol.* **2010**, *28*, 1123.
[13] A. Karimi, M. Navidbakhsh, A. Shojaei, S. Faghihi, *Mater. Sci. Eng., C* **2013**, *33*, 2550.
[14] J. Li, H. Zreiqat, in *Encyclopedia of Biomedical Engineering*, Vol. *1* (Ed: R. Narayan), Elsevier, Amsterdam, Netherland **2019**, Ch 2.
[15] a) Y. Li, J. Zheng, I. M. Bird, R. R. Magness, *Endothelium* **2005**, *12*, 21; b) R. J. Hendrickson, C. Cappadona, E. N. Yankah, J. V. Sitzmann, P. A. Cahill, E. M. Redmond, *J. Mol. Cell. Cardiol.* **1999**, *31*, 619; c) Z. Hu, Y. Xiong, X. Han, C. Geng, B. Jiang, Y. Huo, J. Luo, *PLoS One* **2013**, *8*, e71359; d) Y. Zhang, B. Liao, M. Li, M. Cheng, Y. Fu, Q. Liu, Q. Chen, H. Liu, Y. Fang, G. Zhang, *Cardiovasc. Ther.* **2016**, *34*, 308; e) T. E. Walshe, G. Ferguson, P. Connell, C. O'Brien, P. A. Cahill, *Invest. Ophthalmol. Visual Sci.* **2005**, *46*, 375.
[16] M. He, M. Martin, T. Marin, Z. Chen, B. Gongol, *APL Bioeng.* **2020**, *4*, 010904.
[17] a) A. Sandoo, J. J. V. van Zanten, G. S. Metsios, D. Carroll, G. D Kitas, *Open Cardiovasc. Med. J.* **2010**, *4*, 302; b) P. Rajendran, T. Rengarajan, J. Thangavel, Y. Nishigaki, D. Sakthisekaran, G. Sethi, I. Nishigaki, *Int. J. Biol. Sci.* **2013**, *9*, 1057.
[18] M. Lovett, K. Lee, A. Edwards, D. L. Kaplan, *Tissue Eng., Part B* **2009**, *15*, 353.
[19] B. J. Janssen, J. F. Smits, *Am. J. Physiol.: Regul., Integr. Comp. Physiol.* **2002**, *282*, R1545.
[20] a) J. S. Shahoud, T. Sanvictores, N. R. Aeddula, *Physiology, Arterial Pressure Regulation*, StatPearls, Treasure Island, FL, USA **2019**; b) T. Shrout, D. W. Rudy, M. T. Piascik, *Curr. Opin. Pharmacol.* **2017**, *33*, 41; c) D. B. Wax, S. B. Porter, H.-M. Lin, S. Hossain, D. L. Reich, *J. Cardiothorac. Vasc. Anesth.* **2010**, *24*, 927; d) S. Howell, Y. Sear, D. Yeates, M. Goldacre, J. Sear, P. Foex, *Anaesthesia* **1996**, *51*, 1000.
[21] M. B. Elliott, B. Ginn, T. Fukunishi, D. Bedja, A. Suresh, T. Chen, T. Inoue, H. C. Dietz, L. Santhanam, H.-Q. Mao, *Proc. Natl. Acad. Sci. U. S. A.* **2019**, *116*, 12710.
[22] W. Wu, R. A. Allen, Y. Wang, *Nat. Med.* **2012**, *18*, 1148.
[23] R. Burkhardt, A. Preiss, A. Joss, N. P. J. Lang, *Clin. Oral Implants Res.* **2008**, *19*, 314.
[24] A. Waterhouse, Y. Yin, S. G. Wise, D. V. Bax, D. R. McKenzie, M. M. Bilek, A. S. Weiss, M. K. Ng, *Biomaterials* **2010**, *31*, 8332.
[25] S. Rose, A. Misharin, H. Perlman, *Cytometry, Part A* **2012**, *81*, 343.
[26] A. K. Gaharwar, I. Singh, A. Khademhosseini, *Nat. Rev. Mater.* **2020**, *5*, 686.
[27] a) J. Liu, Y. Qin, Y. Wu, Z. Sun, B. Li, H. Jing, C. Zhang, C. Li, X. Leng, Z. Wang, *Biomater. Sci.* **2019**, *7*, 914; b) Z. Wang, Y. Cui, J. Wang, X. Yang, Y. Wu, K. Wang, X. Gao, D. Li, Y. Li, X.-L. Zheng, *Biomaterials* **2014**, *35*, 5700; c) C. V. Bouten, A. I. Smits, F. P. Baaijens, *Front. Cardiovasc. Med.* **2018**, *5*, 54.
[28] Y. Naito, T. Shinoka, D. Duncan, N. Hibino, D. Solomon, M. Cleary, A. Rathore, C. Fein, S. Church, C. Breuer, *Adv. Drug Delivery Rev.* **2011**, *63*, 312.
[29] M. Hesketh, K. B. Sahin, Z. E. West, R. Z. Murray, *Int. J. Mol. Sci.* **2017**, *18*, 1545.
[30] a) D. H. Madsen, D. Leonard, A. Masedunskas, A. Moyer, H. J. Jürgensen, D. E. Peters, P. Amornphimoltham, A. Selvaraj, S. S. Yamada, D. A. Brenner, *J. Cell Biol.* **2013**, *202*, 951; b) M. Rodrigues, N. Kosaric, C. A. Bonham, G. C. Gurtner, *Physiol. Rev.* **2019**, *99*, 665.
[31] a) E. C. Davis, *J. Histochem. Cytochem.* **1995**, *43*, 1115; b) D. Y. Li, G. Faury, D. G. Taylor, E. C. Davis, W. A. Boyle, R. P. Mecham, P. Stenzel, B. Boak, M. T. Keating, *J. Clin. Invest.* **1998**, *102*, 1783.
[32] M. G. Espinosa, M. C. Staiculescu, J. Kim, E. Marin, J. E. Wagenseil, *J. Biomech. Eng.* **2018**, *140*, 020803.
[33] C.-J. Lin, M. C. Staiculescu, J. Z. Hawes, A. J. Cocciolone, B. M. Hunkins, R. A. Roth, C.-Y. Lin, R. P. Mecham, J. E. Wagenseil, *Circ. Res.* **2019**, *125*, 1006.
[34] Y. Matsuzaki, R. Iwaki, J. W. Reinhardt, Y.-C. Chang, S. Miyamoto, J. Kelly, J. Zbinden, K. Blum, G. Mirhaidari, A. Ulziibayar, T. Shojia, C. K. Breuer, T. Shinoka, *Acta Biomater.* **2020**, *115*, 176.
[35] R. J. Smith, B. Nasiri, J. Kann, D. Yergeau, J. E. Bard, D. D. Swartz, S. T. Andreadis, *Nat. Commun.* **2020**, *11*, 1622.
[36] S. Menashi, J. S. Campa, R. M. Greenhalgh, J. T. Powell, *J. Vascul. Surg.* **1987**, *6*, 578.
[37] M. Zhu, Y. Wu, W. Li, X. Dong, H. Chang, K. Wang, P. Wu, J. Zhang, G. Fan, L. Wang, *Biomaterials* **2018**, *183*, 306.
[38] S. M. Mithieux, A. S. Weiss, *Adv. Protein Chem.* **2005**, *70*, 437.
[39] C. R. Kothapalli, A. Ramamurthi, *Acta Biomater.* **2010**, *6*, 170.
[40] L. Duca, S. Blaise, B. Romier, M. Laffargue, S. Gayral, H. El Btaouri, C. Kawecki, A. Guillot, L. Martiny, L. Debelle, *Cardiovasc. Res.* **2016**, *110*, 298.
[41] a) P. Wu, L. Wang, W. Li, Y. Zhang, Y. Wu, D. Zhi, H. Wang, L. Wang, D. Kong, M. Zhu, *Biomaterials* **2020**, *242*, 119922; b) X. Qiu, B. L.-P. Lee, S. Y. Wong, X. Ding, K. Xu, W. Zhao, D. Wang, R. Sochol, N. Dong, S. Li, *Biomaterials* **2021**, *268*, 120565.
[42] a) D. Y. Li, G. Faury, D. G. Taylor, E. C. Davis, W. A. Boyle, R. P. Mecham, P. Stenzel, B. Boak, M. T. Keating, *J. Clin. Invest.* **1998**, *102*, 1783; b) M. Pezet, M.-P. Jacob, B. Escoubet, D. Gheduzzi, E. Tillet, P. Perret, P. Huber, D. Quaglino, R. Vranckx, D. Y. Li, *Rejuvenation Res.* **2008**, *11*, 97.
[43] a) G. Faury, M. Pezet, R. H. Knutsen, W. A. Boyle, S. P. Heximer, S. E. McLean, R. K. Minkes, K. J. Blumer, A. Kovacs, D. P. Kelly, *J. Clin. Invest.* **2003**, *112*, 1419; b) J. E. Wagenseil, N. L. Nerurkar, R. H. Knutsen, R. J. Okamoto, D. Y. Li, R. P. Mecham, *Am. J. Physiol.: Heart Circ. Physiol.* **2005**, *289*, H1209.
[44] S. G. Wise, S. M. Mithieux, A. S. Weiss, *Adv. Protein Chem. Struct. Biol.* **2009**, *78*, 1.
[45] a) S. M. Mithieux, A. S. Weiss, *Acta Biomater.* **2017**, *52*, 33; b) M. G. Mitzmacher, S. M. Mithieux, A. S. Weiss, C. K. Hee, R. Daniels, *J. Drugs Dermatol.* **2020**, *19*, 1166.